










RESEARCH ARTICLE

Raman shifts in MBE-grown $\text{Si}_x\text{Ge}_{1-x-y}\text{Sn}_y$ alloys with large Si content

Jon Schlipf¹  | Henriette Tetzner²  | Davide Spirito²  |
Costanza L. Manganelli²  | Giovanni Capellini^{2,3}  | Michael R. S. Huang⁴ |
Christoph T. Koch⁴  | Caterina J. Clausen⁵  | Ahmed Elsayed⁵ |
Michael Oehme⁵ | Stefano Chiussi⁶  | Jörg Schulze⁵ | Inga A. Fischer^{1,5} 

¹Department of Experimental Physics and Functional Materials, BTU Cottbus–Senftenberg, Cottbus, Germany

²Department of Material Research–Semiconductor Optoelectronics, IHP–Leibniz-Institut für innovative Mikroelektronik, Frankfurt, Germany

³Dipartimento di Scienze, Università degli Studi Roma Tre, Rome, Italy

⁴AG Strukturforchung/Elektronenmikroskopie, HU Berlin, Berlin, Germany

⁵Institut für Halbleitertechnik, Universität Stuttgart, Stuttgart, Germany

⁶CINTECX, Universidade de Vigo, Vigo, Spain

Correspondence

Jon Schlipf, Department of Experimental Physics and Functional Materials, BTU Cottbus–Senftenberg, Cottbus, Brandenburg, Germany.
Email: jon.schlipf@b-tu.de

Funding information

Deutsche Forschungsgemeinschaft, Grant/Award Numbers: KO 2911/13-1, CA 1474/3-1, FI 1511/4-1

Abstract

We examine the Raman shift in silicon–germanium–tin alloys with high silicon content grown on a germanium virtual substrate by molecular beam epitaxy. The Raman shifts of the three most prominent modes, Si–Si, Si–Ge, and Ge–Ge, are measured and compared with results in previous literature. We analyze and fit the dependence of the three modes on the composition and strain of the semiconductor alloys. We also demonstrate the calculation of the composition and strain of $\text{Si}_x\text{Ge}_{1-x-y}\text{Sn}_y$ from the Raman shifts alone, based on the fitted relationships. Our analysis extends previous results to samples lattice matched on Ge and with higher Si content than in prior comprehensive Raman analyses, thus making Raman measurements as a local, fast, and nondestructive characterization technique accessible for a wider compositional range of these ternary alloys for silicon-based photonic and microelectronic devices.

KEYWORDS

asymmetric lineshape, Group IV materials, molecular beam epitaxy, semiconductor alloy, SiGeSn

1 | INTRODUCTION

Ge and SiGe alloys have been successfully integrated into commercial complementary metal–oxide–semiconductor (CMOS) processes for applications that range from

boosting transistor performance^[1] to enabling optical on-chip functionality.^[2] Recently, the possible addition of another Group IV semiconductor, tin (Sn), into the SiGe material system has attracted large interest, mainly due to the possibility to realize a direct-bandgap

This is an open access article under the terms of the Creative Commons Attribution-NonCommercial-NoDerivs License, which permits use and distribution in any medium, provided the original work is properly cited, the use is non-commercial and no modifications or adaptations are made.

© 2021 The Authors. *Journal of Raman Spectroscopy* published by John Wiley & Sons Ltd.

semiconductor for a sufficiently large Sn content (about 10% in GeSn).^[3,4] Indeed, the binary $\text{Ge}_{1-y}\text{Sn}_y$ and ternary $\text{Si}_x\text{Ge}_{1-x-y}\text{Sn}_y$ alloys can potentially extend the application range of Group IV materials. Besides the possibility offered to fabricate integrated light sources,^[3] their high hole mobility, as compared with Si or Ge, is promising for high-speed electronic devices.^[5] In addition, the smaller bandgap and larger absorption coefficient can enable Group IV photodetectors with cutoff wavelengths further into the infrared and allow thinner active layers.^[6,7] However, the large lattice mismatch existing between Sn and Si and Ge (19% and 15%, respectively) together with the limited solid solubility of Sn poses important challenges in the deposition of epitaxial (Si)GeSn layers. In particular, if one aims at depositing them on Si substrates, as required by integration into mainstream Si microelectronics, a large heteroepitaxial strain buildup must be taken into account.

It is worth noting that high Sn-content $\text{Si}_x\text{Ge}_{1-x-y}\text{Sn}_y$ layers can be grown lattice matched on Ge^[8,9] by choosing the layer composition as $x(a_{\text{Ge}} - a_{\text{Si}}) = y(a_{\text{Sn}} - a_{\text{Ge}})$. This enables decoupling the lattice constant from the (opto)electronic properties, opening pathways towards promising applications in nanoelectronics and photonics.^[6,7,10–12] For further development of $\text{Si}_x\text{Ge}_{1-x-y}\text{Sn}_y$ growth techniques and devices, it is crucial to correctly characterize their composition and lattice properties because those parameters decisively influence both electronic and optoelectronic characteristics.^[13]

Although material composition and strain can be measured with a high degree of accuracy using Rutherford backscattering spectrometry (RBS) and X-ray diffraction (XRD), these techniques are time-consuming and give information averaged over a relatively large area of the sample, much larger than the typical device size. This makes them unsuitable for the characterization of sub-micrometer-scale variations of composition and strain, which occur, for example, in selective semiconductor growth processes or after structuring. Transmission electron microscopy (TEM) combined with energy-dispersive X-ray spectroscopy (EDXS) or electron nanodiffraction provide composition and lattice information with nanometer-scale resolution, but those techniques require the destruction of the analyzed sample. In contrast, micro-Raman spectroscopy can provide submicrometer resolution and high speed and is nondestructive. As such, micro-Raman spectroscopy can be a valuable tool to study material composition and strain in $\text{Si}_x\text{Ge}_{1-x-y}\text{Sn}_y$ layers. In order to measure composition and strain from Raman spectroscopy, empirical relations between peak positions in the Raman spectra and material composition as well as strain have to be derived. Previous studies on the Raman shifts of $\text{Si}_x\text{Ge}_{1-x-y}\text{Sn}_y$ alloys have been

conducted for Si fractions of up to 20%.^[14,15] An extension to $\text{Si}_x\text{Ge}_{1-x-y}\text{Sn}_y$ alloys with higher Si content, as they can be obtained by molecular beam epitaxy (MBE), is not necessarily straightforward. It was previously found for material properties such as critical points in the optical density of states^[13] that a compositional dependence established for alloys with low Si and Sn content can fail to provide an accurate description of the behavior for $\text{Si}_x\text{Ge}_{1-x-y}\text{Sn}_y$ alloys with high Si content. As a result, the relationship between composition and strain parameters and Raman spectra for $\text{Si}_x\text{Ge}_{1-x-y}\text{Sn}_y$ alloys with high Si content does not necessarily have to follow the trends observed for lower Si and Sn fractions.^[14,15] This motivates our work to extend the accessible parameter range by investigating MBE-grown $\text{Si}_x\text{Ge}_{1-x-y}\text{Sn}_y$ alloys featuring larger Si fractions (up to 46%) (Figure S1) and combine Raman results with an exhaustive complementary characterization of composition and structure through RBS, XRD, and TEM/EDS.

2 | GROWTH AND CHARACTERIZATION

We grew four samples featuring a 100-nm $\text{Si}_x\text{Ge}_{1-x-y}\text{Sn}_y$ layer with increasing Si and Sn content by MBE on a 100-nm-thick relaxed $\text{p}^{++}\text{-Ge/Si}(100)$ layer, using 4-in. substrates. The samples were grown at a rate of 1.0 nm/s and a substrate temperature of 160°C. Si was evaporated via electron beam, whereas Ge and Sn came from effusion cells. Details of the growth procedure, including the virtual substrate, are reported in Fischer et al.^[13] The nominal compositions of the $\text{Si}_x\text{Ge}_{1-x-y}\text{Sn}_y$ layers were chosen in such a way that lattice matching with the Ge virtual substrate was approximately achieved, according to $x(a_{\text{Ge}} - a_{\text{Si}}) = y(a_{\text{Sn}} - a_{\text{Ge}})$, where x and y stand for the Si and Sn atomic fractions, and a_{Si} , a_{Ge} , and a_{Sn} are the lattice constants of the three elements (Figure S1). These samples with relatively low strain, grown with the aim of decoupling the lattice constant from the (opto)electronic properties, also facilitate the Raman analysis due to a relatively low strain-related peak shift. The samples were grown with nominal Sn fractions of 5%, 7.5%, 10%, and 12.5% and corresponding Si fractions of 18%, 27.5%, 37%, and 46%, respectively. We also note that the position of the Ge and Sn effusion cells in the MBE setup with respect to the (rotating) wafer caused a variation of the Ge and Sn content over the wafer surface in radial direction, which gave us access to a larger variation in sample composition. Compositional information, therefore, was obtained for each sample from three different positions on the wafer, that is, at the center (I), at half the radius (II), and at the edge (III) of each wafer.

For all samples, XRD measurements were performed, and lattice constants were determined on the basis of rocking curves as well as reciprocal space maps (RSMs). For each sample, one RSM and three rocking curves for three positions of interest on the sample were measured.^[9,13]

To investigate the crystal quality, samples were characterized by scanning TEM (STEM) in high-angle annular dark-field (HAADF) mode, which can provide compositional information (the image contrast is proportional to $Z^{1.7}$, where Z is the atomic number). Furthermore, an EDXS analysis was conducted in STEM mode to examine the compositional distribution as well as the homogeneity of the grown $\text{Si}_x\text{Ge}_{1-x-y}\text{Sn}_y$ thin films.

All four samples were characterized by micro-Raman spectroscopy at room temperature at three positions on the wafer ((I)–(III)). It has been shown previously^[15] that the use of two Raman wavelengths with different penetration depths can be helpful in the sample analysis, disentangling the contributions from the three layers on the sample; 532- and a 633-nm lasers were available in two distinct setups and employed for characterization.

The 633-nm Raman spectra were obtained with a Renishaw inVia Microscope system with a 633-nm He-Ne laser as excitation source and a power of 10 mW. The setup had a range of 220 to 795 cm^{-1} and a step size of 1.1 cm^{-1} . Laser light was focused on the sample through a 50 \times objective to a spot size of <1 μm . The scattered light from the sample was collected through the same microscope and measured with a spectrometer with 1800-line/mm grating. A Renishaw charge-coupled device (CCD) camera was used as detector. The 532-nm Raman spectra were obtained with a different Renishaw inVia system, equipped with a 532-nm diode laser as excitation source. The power on the sample was <1 mW. Light was focused and collected with a 50 \times objective, resulting in a laser spot diameter of <1 μm . The spectrometer featured 2400-line/mm grating. The 532-nm Raman spectra were recorded in a range between 180 and 515 cm^{-1} with a step size of 1.2 cm^{-1} .

We note that our equipment did not allow for polarization-resolved Raman measurements. However, because composition of our samples was targeting a complete relaxation of the homogeneous epitaxial films, we do not expect any polarization-dependent behavior in the modes evaluated in this work.

3 | RESULTS

3.1 | Composition and structure using state-of-the-art techniques

All samples were characterized with state-of-the-art techniques as a foundation to base our micro-Raman

spectroscopy analysis on. Quantitative information on composition for all samples was obtained from RBS measurements, as published elsewhere.^[9,13] We note that the RUMP simulation software was used for fitting of the random RBS spectra with normalization with respect to the Ge buffer, as recommended by Xu et al.^[16] An example fit and detailed discussion is provided by Wendav et al.^[9] Table 1 shows the compositional information for the three different positions on the wafer, that is, at the center (I), at half the radius (II), and at the edge (III) of each wafer. For all samples, the Sn content as obtained from RBS measurements was found to increase from the center towards the edge of the wafer (Table 1). The lattice constant and strain were measured by XRD and, together with detailed ellipsometric characterizations of transition energies, were discussed previously.^[9,13] Additional XRD rocking curves of Samples A and C are included in Figure S2 and discussed in more detail there. For all samples, the out-of-plane lattice constant increases from the center to the edge of the wafer (Table 1).

From the in-plane (a_p) and out-of-plane (a_s) lattice constants of the structure obtained from XRD, the theoretical unstrained lattice constant a_0 was calculated assuming tetragonal lattice distortion. The elastic coefficients of the elemental semiconductors Si, Ge, and α -Sn were taken from literature.^[17] For alloys, we interpolated the ratios of elastic coefficients C_{12}/C_{11} .^[17] The XRD results for the $\text{Si}_x\text{Ge}_{1-x-y}\text{Sn}_y$ layer can be compared against the predictions of Vegard's law based on the RBS composition data. Only slight deviations of up to 1.6 pm are found between the predictions of Vegard's law and the actual lattice constants (Table 1). Even better agreement could be found between our XRD results and an empirical nonlinear model discussed by Xu et al.,^[16] which includes bowing parameters for the lattice constant of $\text{Si}_x\text{Ge}_{1-x-y}\text{Sn}_y$ alloys.^[16] This indicates the applicability of bowing parameters obtained from binary alloys to the ternary $\text{Si}_x\text{Ge}_{1-x-y}\text{Sn}_y$ system, even in the regime where both x_{Si} and y_{Sn} are high.

A cross-sectional STEM image of the complete heterostructure in HAADF mode and the EDXS maps of the ternary alloy with part of the Ge virtual substrate are shown for Sample C in Figure S3, along with extended description. They confirm low-defect epitaxial growth of $\text{Si}_x\text{Ge}_{1-x-y}\text{Sn}_y$ on Ge with excellent homogeneity.

After the determination of structure, strain, and composition of each of the samples through the combination of these techniques, we proceeded to the characterization by micro-Raman spectroscopy and elaborated a set of empirical relations that enable the determination of material composition and strain in lattice-matched $\text{Si}_x\text{Ge}_{1-x-y}\text{Sn}_y$ alloys with high Si content, based on a Raman analysis alone.

Sample	Position	x_{Si} (%)	y_{Sn} (%)	a_p (nm)	a_s (nm)	a_0 (nm)	a_{veg} (nm)	a_{nl} (nm)	ϵ (%)
A	I	18.5	5.5	0.5664	0.5649	0.5657	0.5662	0.5658	0.11
	II	19.3	5.7	0.5664	0.5655	0.5660	0.5662	0.5658	0.07
	III	19.5	6.2	0.5664	0.5660	0.5662	0.5665	0.5661	0.03
B	I	26.5	7.5	0.5660	0.5647	0.5654	0.5660	0.5655	0.10
	II	26.2	7.8	0.5659	0.5650	0.5655	0.5664	0.5659	0.07
	III	26.2	8.3	0.5659	0.5658	0.5658	0.5668	0.5663	0.01
C	I	41.8	8.7	0.5661	0.5605	0.5636	0.5636	0.5630	0.44
	II	41.8	9.0	0.5661	0.5608	0.5638	0.5638	0.5632	0.42
	III	42.2	9.8	0.5661	0.5613	0.5640	0.5644	0.5638	0.38
D	I	46.1	12.4	0.5658	0.5636	0.5648	0.5657	0.5651	0.17
	II	46.3	12.7	0.5657	0.5640	0.5650	0.5659	0.5653	0.13
	III	46.0	13.5	0.5657	0.5644	0.5651	0.5666	0.5660	0.11

TABLE 1 Structural characterization results at the three positions on a 4-in. wafer for all samples: Si and Sn atomic fractions x_{Si} and y_{Sn} , in-plane and out-of-plane lattice constants a_p and a_s , theoretical unstrained lattice constant a_0 , prediction of Vegard's law a_{veg} , nonlinear prediction a_{nl} ,¹⁶ and in-plane strain ϵ

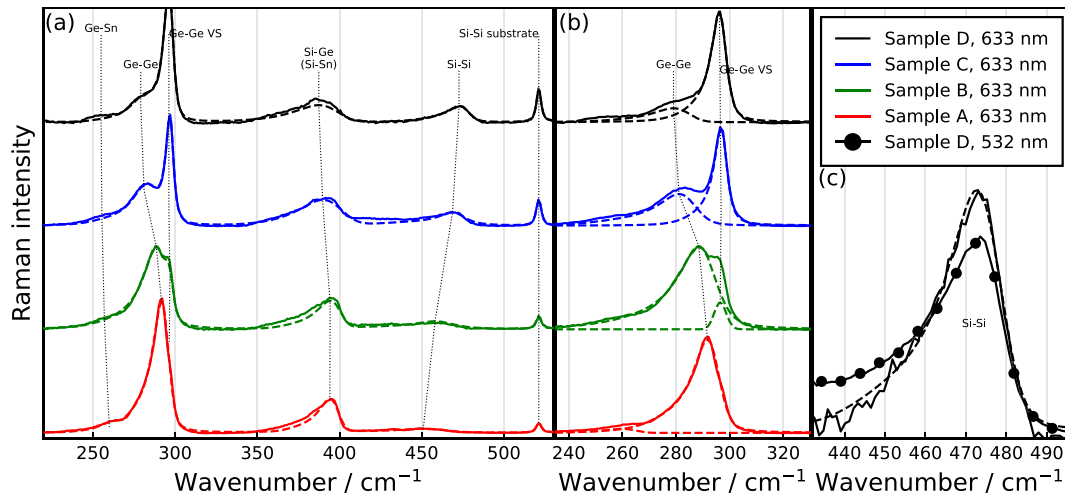


FIGURE 1 Baseline-corrected Raman spectra measured at the center (solid) and fits (dashed) for all four samples characterized in this work. (a) Full 633-nm spectra. (b) Overlap of the Ge-Ge peaks of the $Si_xGe_{1-x-y}Sn_y$ layer and Ge VS. (c) Si-Si peak on Sample D for both excitation wavelengths

3.2 | Raman spectroscopy

Information on vibrational modes in our $Si_xGe_{1-x-y}Sn_y$ layers was obtained from Raman spectroscopy using two different laser wavelengths. In our samples, the Raman modes that can in principle be observed are the Si-Si mode from the Si wafer, the Ge-Ge mode from the Ge VS, and the Ge-Sn, Ge-Ge, Si-Ge, Si-Sn, and Si-Si modes from the $Si_xGe_{1-x-y}Sn_y$ layer. The absence of the VS Ge-Ge mode and the substrate Si-Si mode from the 532-nm Raman spectra is a consequence of the wavelength-dependent attenuation. Although the precise attenuation length in our $Si_xGe_{1-x-y}Sn_y$ alloys is

unknown and likely to be a function of composition, we can take spectroscopic data for Ge as the basis for a qualitative comparison: the 633-nm laser excitation has a Raman penetration depth (half attenuation length) of 35 nm in Ge.^[18] The radiation penetrated to the Si substrate, leading to a weak Si-Si peak at $\sim 520\text{ cm}^{-1}$ (Figure 1a). We used this peak as an internal reference for the wavenumber calibration in all 633-nm samples and set it to 521.2 cm^{-1} . This value was selected for consistency with Shin et al.,^[19] on which the model for the relations between composition, strain, and Raman peak positions employed here is based. In contrast, given its much shorter Raman penetration depth of 10 nm,^[17] the

532-nm laser did not penetrate into the Ge VS and Si substrate, and only peaks from the $\text{Si}_x\text{Ge}_{1-x-y}\text{Sn}_y$ layer are visible in the spectra.

Before we provide a quantitative treatment of our measurement results for the strongest modes (Ge–Ge, Si–Ge, and Si–Si), we briefly discuss the qualitative effects of compositional changes on all observable modes, starting from those with the largest Raman shift (Figure 1).

Compared with the Si–Si substrate mode, the Si–Si mode originating from the $\text{Si}_x\text{Ge}_{1-x-y}\text{Sn}_y$ layer is noticeably shifted to the 450- to 470- cm^{-1} range. In a previous investigation,^[15] this mode was reported to result in two Si–Si peaks with different intensities visible in the spectrum, where the weak one could be found at wavenumbers $\sim 15\text{ cm}^{-1}$ smaller than the position of the strong one. In our samples, this weak peak is visible in Samples A and B, whereas the strong Si–Si peak could be observed in all samples. This is in agreement with a previous study,^[15] which only observed the weak Si–Si mode for Sn fractions $< 7\%$. We therefore exclusively investigate the strong peak and refer to it as the Si–Si peak. The peak position increases with increasing Si fraction (Figure 1a). As far as Si–Si mode is concerned, an increase in Si content leads to a shift to higher wavenumbers, whereas an increase in Sn content is expected to induce a shift to lower wavenumbers.^[15] Although Si and Sn incorporations have diametrically opposed effects on the Si–Si peak position, the effect of Si dominates here, shifting the resonance towards higher wavenumbers. As we can see in Figure 1c, the 532- and 633-nm results perfectly match for this Si–Si mode that is particularly difficult to evaluate, due to the weak signal as compared with the background, even for the sample with highest Si content. We therefore chose to continue the investigation with the 633-nm spectra because this wavelength has been reported to enable the best mode identification in similar layer structures.^[15] Furthermore, the Si substrate peak visible in the 633-nm spectra can be used as an internal calibration to verify that no measurement artifacts affect the spectra.

The peaks between 380 and 390 cm^{-1} can be attributed to the Si–Ge and Si–Sn modes,^[15] which have also been found to overlap in previous investigations. Depending on sample composition, those peaks cannot always be clearly separated (Figure 1a): the Si–Ge mode dominates in Sample A with the highest Ge content; however, the Si–Sn mode becomes more prominent as Si and Sn contents are increased. For the Si–Ge mode, the dependence of the peak position on alloy composition can be expected to be highly nonlinear; Shin et al.^[19] have given a polynomial fit for the behavior in SiGe alloys.

In contrast to the Si–Si modes at 520 cm^{-1} and at 450 to 470 cm^{-1} , where contributions from the substrate

and from the $\text{Si}_x\text{Ge}_{1-x-y}\text{Sn}_y$ layer appear as distinct peaks for all samples, the Ge–Ge modes from the substrate and the $\text{Si}_x\text{Ge}_{1-x-y}\text{Sn}_y$ layer overlap for all samples investigated here, at 270 to 300 cm^{-1} . Indeed, for Sample A with the highest Ge content, only one Ge–Ge mode is visible and originates from the $\text{Si}_x\text{Ge}_{1-x-y}\text{Sn}_y$ layer, whereas the Ge–Ge mode from the VS also becomes visible as a distinct peak at a fixed position ($(296.6 \pm 0.1)\text{ cm}^{-1}$) for Samples B–D (Figure 1b). With decreasing Ge content, the intensity of the Ge–Ge peak originating from the $\text{Si}_x\text{Ge}_{1-x-y}\text{Sn}_y$ layer can also be seen to decrease. Furthermore, from previous investigations,^[14,15] it is known that the increase of both the Si and Sn fraction causes the Ge–Ge mode to shift towards smaller wavenumbers. We observe the same trend in our samples.

Finally, although the Ge–Sn peak is visible at $\sim 255\text{ cm}^{-1}$ as a weak shoulder in all samples, the Sn–Sn mode originating from the $\text{Si}_x\text{Ge}_{1-x-y}\text{Sn}_y$ layer is not visible due to its position at around 190 cm^{-1} , below the lowest Raman shift detectable by our setups.^[15]

3.3 | Compositional dependencies of Raman shifts

For our samples, extracting the peak positions for the signal originating from the Ge–Sn and Si–Sn modes was not possible for all cases. Thus, our quantitative analysis focuses on results for the more prominent Ge–Ge, Si–Ge, and Si–Si modes.

In order to extract the peak positions, all peaks were fitted using an asymmetrically broadened pseudo-Voigt distribution^[20] (Figure 1). As compared with the commonly used exponentially modified Gaussian distribution, this reflects the broadening processes that lead to Lorentzian lineshapes as well. Another advantage is that it directly yields the peak maximum ω_0 as a fit parameter, without any additional need for analytic or numeric correction.^[20] We employed an asymmetric Whittaker smoother^[21,22] for baseline correction of the recorded spectra. Fits are obtained from the original Raman data via the Levenberg–Marquardt algorithm.^[23] The resulting peak positions ω_0 for the vibrational modes are shown in Table 2.

Empirical relationships between peak positions and sample composition as well as strain enable quantitative Raman analysis. There have been detailed previous studies on the Raman peak positions of $\text{Si}_x\text{Ge}_{1-x-y}\text{Sn}_y$ by D'Costa et al.^[14] as well as by Fournier-Lupien et al.^[15] Both works take into account composition measured by RBS and strain determined from XRD results and give linear dependencies of the peak positions corresponding

TABLE 2 Six hundred thirty-three-nanometer Raman shifts of the three most prominent modes at the center (I), half radius (II), and edge (III) of all four samples

	ω_{Ge-Ge} (cm^{-1})			ω_{Si-Ge} (cm^{-1})			ω_{Si-Si} (cm^{-1})		
	I	II	III	I	II	III	I	II	III
A	291.7 ± 0.4	291.9 ± 0.3	291.7 ± 0.3	394.1 ± 0.4	394.3 ± 0.4	394.5 ± 0.4	450.9 ± 2.8	450.3 ± 3.2	451.5 ± 2.8
B	288.5 ± 0.5	288.3 ± 0.9	287.7 ± 1.1	394.3 ± 0.4	394.3 ± 0.7	393.8 ± 0.6	458.1 ± 1.3	457.2 ± 2.9	458.0 ± 2.1
C	281.1 ± 0.6	280.4 ± 0.7	280.4 ± 0.7	392.3 ± 0.4	392.1 ± 0.4	391.9 ± 0.5	468.7 ± 0.7	468.9 ± 0.6	469.6 ± 0.6
D	279.1 ± 0.9	278.6 ± 0.4	278.8 ± 0.5	387.4 ± 0.6	387.4 ± 0.3	387.3 ± 0.3	472.7 ± 0.5	472.5 ± 0.3	472.7 ± 0.3

to the Si-Si, Si-Ge, and Ge-Ge vibrational modes. In contrast to those earlier works, here we exclusively examine $\text{Si}_x\text{Ge}_{1-x-y}\text{Sn}_y$ films grown lattice matched on a relaxed Ge layer, which enables the incorporation of a higher Si content into the alloy (up to 0.46 in our samples). Our investigation, thus, extends the Raman analysis of $\text{Si}_x\text{Ge}_{1-x-y}\text{Sn}_y$ alloys to samples with higher Si content compared with samples used in earlier works, which only feature Si contents of ≤ 0.2 . For a comprehensive analysis, we take into account not only data obtained from our samples but also measurement data reported in those previous studies^[14,15] in order to obtain the best possible fit for a wide range of alloy composition and strain.

We employ a linear approach for the dependence of the vibrational modes on composition and strain, as introduced by Fournier-Lupien et al.,^[15]

$$\omega_{Ge-Ge} = \omega_{Ge-Ge}^{Ge} - a_{Ge-Ge}^{GeSi}x - a_{Ge-Ge}^{GeSn}y + b_{Ge-Ge}\epsilon, \quad (1)$$

$$\omega_{Si-Ge} = \omega_0(1-x-y) - a_{Si-Ge}y + b_{Si-Ge}\epsilon, \quad (2)$$

$$\omega_{Si-Si} = \omega_{Si-Si}^{Si} - a_{Si-Si}^{GeSi}(1-x-y) - a_{Si-Si}^{SiSn}y + b_{Si-Si}\epsilon, \quad (3)$$

$$\omega_0(z) = 400 + 22.07z - 36.14z^2 + 83.73z^3 - 88.54z^4. \quad (4)$$

Here, $\omega_{Ge-Ge}^{Ge} = 300.2 \text{ cm}^{-1}$ and $\omega_{Si-Si}^{Si} = 521.2 \text{ cm}^{-1}$ are the wavenumbers of the modes in a pure Ge and Si crystal, whereas $\omega_0(z)$ is a polynomial expression based on experimental results, where $z = 1 - x - y$ stands for the Ge fraction. This expression was also employed in the two previous analyses.^[14,15] Together with the linear coefficient for the Ge-Ge mode in a SiGe alloy, $a_{Ge-Ge}^{GeSi} = 19.37 \text{ cm}^{-1}$, the polynomial is taken from Shin et al.^[19] The parameter ϵ refers to the in-plane strain.

In analogy to SiGe, the in-plane strain shift coefficients b_{Ge-Ge} , b_{Si-Ge} and b_{Si-Si} are expected to depend on composition.^[24] However, because the relationships are not known for $\text{Si}_x\text{Ge}_{1-x-y}\text{Sn}_y$ and they cannot be fitted with

reasonable accuracy from our dataset, we chose to assume constant coefficients in our mathematical model. Although previous investigations^[14,15] were based on values adapted from SiGe,^[25,26] we prefer to fit them instead. The literature values are specified with large margins of error and were obtained from binary alloys, so we included them among the fit parameters in a first analysis. Because most samples analyzed here have relatively low strain, the resulting in-plane strain shift coefficients have large error bars. The model can consistently fit all available Raman data (Figure 2), and an overview of the values obtained for the parameters as well as a comparison with previous results is shown in Table 3.

We also conducted the same analysis with the in-plane strain coefficients fixed at the values used in previous work (Table 3). The last two columns do not differ much, and their error bars overlap, because the low strain in the samples examined here has a smaller influence on the Raman shift than composition.

For the Ge-Ge peak, we find a Sn composition coefficient $a_{Ge-Ge}^{GeSn} = (89.9 \pm 2.9) \text{ cm}^{-1}$ and an in-plane strain shift coefficient $b_{Ge-Ge} = (-402 \pm 49) \text{ cm}^{-1}$. We did not observe any evidence for higher order terms for Equation (1): the value for a_{Ge-Ge}^{GeSn} agrees very well with the results of previous studies,^[14,15] and similar values for b_{Ge-Ge} have been observed in the past.^[25] Because of this, our fit for this peak does not significantly improve on the root-mean-square (rms) error that we employed as a metric of the fit accuracy. We obtain an rms error of 1.06 cm^{-1} , as compared with the accuracy of the predictions from previous works on the whole dataset, being 1.14 cm^{-1} (D'Costa et al.^[14]) and 1.09 cm^{-1} (Fournier-Lupien et al.^[15]). For this as well as the other samples, the relative error in the in-plane strain coefficient is quite high, because the derivative of the peak positions with respect to it is relatively low. Varying the in-plane strain coefficients thus only slightly affects the quality of the fit, as compared with the composition coefficients.

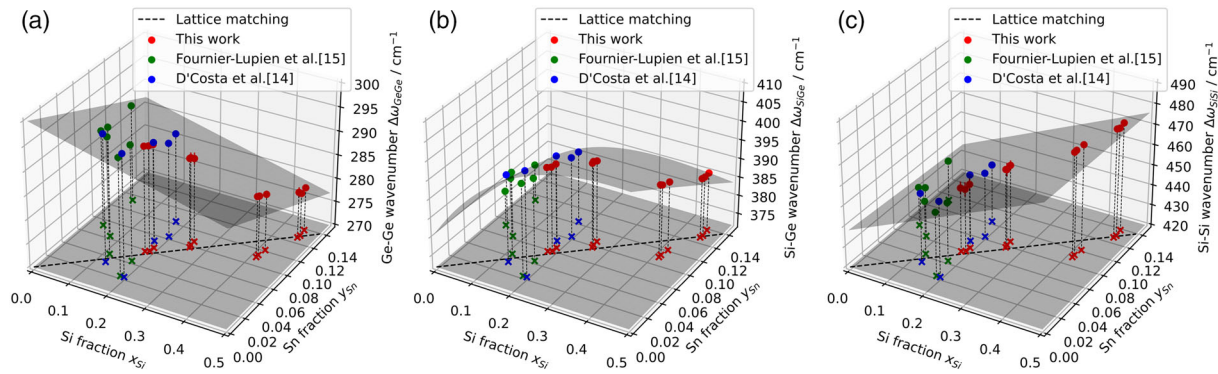


FIGURE 2 Fit of the Raman peak position of the (a) Ge–Ge, (b) Si–Ge, and (c) Si–Si modes as a function of composition and strain. The contribution of the strain is subtracted from the experimental data to facilitate display in a three-dimensional plot

TABLE 3 Comparison of the composition and in-plane strain shift coefficients (in cm^{-1}) determined here with literature values

	Binary alloys	D'Costa et al. ^[14]	Fournier-Lupien et al. ^[15]	This work	This work, <i>b</i> not fitted
$a_{\text{Ge-Ge}}^{\text{GeSi}}$	19.4 ^[19]	17.1 ± 2.6	19.2	19.4 ^[19]	19.4 ^[19]
$a_{\text{Ge-Ge}}^{\text{GeSn}}$	88 ± 3 ^[27]	94.0 ± 7.1	93.5	89.9 ± 2.9	90.0 ± 2.8
$a_{\text{Si-Ge}}$	—	110	166	145.6 ± 3.0	146.6 ± 3.8
$a_{\text{Si-Si}}^{\text{GeSi}}$	67.9 ^[19]	71.2 ± 1.7	80	82.9 ± 0.5	82.9 ± 0.5
$a_{\text{Si-Si}}^{\text{SiSn}}$	—	213 ± 12	160	107.7 ± 4.7	110.2 ± 4.7
$b_{\text{Ge-Ge}}$	−415 ^[26]	−415 ^[26]	−415 ^[26]	$−402 \pm 49$	−415 ^[26]
$b_{\text{Si-Ge}}$	−575 ^[25]	−575 ^[25]	−575 ^[25]	$−389 \pm 51$	−575 ^[25]
$b_{\text{Si-Si}}$	−815 ^[25]	−984	−984 ^[15]	$−607 \pm 96$	−984 ^[14]

For the Si–Ge peak, we obtain $a_{\text{Si-Ge}} = (145.3 \pm 3.0) \text{ cm}^{-1}$ and $b_{\text{Si-Ge}} = (-389 \pm 51) \text{ cm}^{-1}$. The in-plane strain shift coefficient agrees well with results from previous work.^[15] Thus, the polynomial equation reported by Shin et al.^[19] appears to provide a good approximation also for ternary alloys. Because nonlinear relations between the Raman shift and the Sn concentration might also be possible, we attempted to fit models in which the second-order terms $c_{\text{Si-Ge}}xy$ and $a_{2,\text{Si-Ge}}y^2$ were added to Equation (2). However, those fits yielded large relative uncertainties with the available data, so we did not find any evidence for the existence of these nonlinearities. Without these terms and terms of even higher order, our Equations (2) and (4) fit the data within the margin of error, and we consider them sufficient. Although it is a potential challenge in peak fitting that the Si–Ge mode can overlap with the Si–Sn mode,^[15] the good agreement with the polynomial by Shin et al.^[19] corroborates our peak fit results. Although our model does not fit the experimental results of Fournier-Lupien et al.^[15] as well as their model obtained from their dataset alone (the rms error in the predicted peak position increased by 17%), we obtained a reduction in the

rms error by a factor of 2 to 1.11 cm^{-1} for the full dataset. Furthermore, our model provides an improved fit to the Si–Ge peaks reported by D'Costa et al.^[14] compared with Fournier-Lupien et al.^[15]; that is, the rms error is reduced by a factor of 2.

The Si–Si peak proved to be the most difficult one to assess, because the Raman peaks were weak and introduced a rather large uncertainty. In contrast with the Ge–Ge mode, here, both composition parameters $a_{\text{Si-Si}}^{\text{GeSi}}$ and $a_{\text{Si-Si}}^{\text{SiSn}}$ had to be fitted because the former does not match the behavior in a SiGe alloy as examined by Shin et al.^[19] We obtained $a_{\text{Si-Si}}^{\text{GeSi}} = (82.9 \pm 0.5) \text{ cm}^{-1}$ and $a_{\text{Si-Si}}^{\text{SiSn}} = (107.7 \pm 4.7) \text{ cm}^{-1}$ in good agreement with the results of Fournier-Lupien et al.^[15] We note that $a_{\text{Si-Si}}^{\text{GeSi}}$ shows a significant deviation of around 10% from binary SiGe alloy values (Table 3). The higher $a_{\text{Si-Si}}^{\text{GeSi}}$ value appears to be a unique feature of ternary alloys. Although a detailed explanation is beyond the scope of this work, this could be an interesting aspect for future analysis. The in-plane strain shift coefficient was found to be $b_{\text{Si-Si}} = (-608 \pm 44) \text{ cm}^{-1}$. As for the other two peaks, we attempted to fit models with higher order terms, but the result did not significantly improve the

		RBS/XRD			Raman		
		x_{Si} (%)	y_{Sn} (%)	ϵ (%)	x_{Si} (%)	y_{Sn} (%)	ϵ (%)
A	I	18.5	5.5	0.15	16.9 ± 1.0	5.8 ± 2.1	-0.0 ± 0.5
	II	19.3	5.7	0.09	16.8 ± 0.8	5.2 ± 2.4	0.1 ± 0.6
	III	19.5	6.2	0.04	17.4 ± 0.8	5.8 ± 2.0	0.0 ± 0.5
B	I	26.5	7.5	0.13	24.8 ± 1.3	8.7 ± 0.8	-0.2 ± 0.2
	II	26.2	7.8	0.09	24.7 ± 2.4	8.2 ± 1.6	-0.1 ± 0.5
	III	26.2	8.3	0.01	25.7 ± 2.5	8.8 ± 1.3	-0.1 ± 0.4
C	I	41.8	8.7	0.55	45.1 ± 1.6	7.8 ± 0.8	0.8 ± 0.3
	II	41.8	9.0	0.52	45.5 ± 1.4	7.8 ± 0.8	0.9 ± 0.2
	III	42.2	9.8	0.47	46.9 ± 1.8	7.7 ± 1.0	0.9 ± 0.3
D	I	46.1	12.4	0.22	46.9 ± 2.4	12.3 ± 1.3	0.2 ± 0.4
	II	46.3	12.7	0.17	48.0 ± 1.1	11.7 ± 0.6	0.4 ± 0.2
	III	46.0	13.5	0.14	47.5 ± 1.3	12.2 ± 0.7	0.3 ± 0.2

Abbreviations: RBS, Rutherford backscattering spectrometry; XRD, X-ray diffraction.

accuracy, while yielding large relative errors ($\pm 150\%$) in the parameters. Our fit for the Si–Si peak yields an rms error of 1.81 cm^{-1} , for the whole dataset, whereas the models in previous works yield 5.4 cm^{-1} (D'Costa et al.^[14]) and 3.6 cm^{-1} (Fournier-Lupien et al.^[15]). Our fit has the largest rms deviation (3.0 cm^{-1}) from experimental measurements for the dataset provided by D'Costa et al.^[14] We note that employing an excitation source with a lower wavelength could be a means to improve the signal intensity originating from the Si–Si mode; however, this was not possible in our Raman setup.

We found that it is feasible to obtain composition and strain of the $\text{Si}_x\text{Ge}_{1-x-y}\text{Sn}_y$ layers from the Raman shifts of the three most prominent modes using the equation system (1–4) with the parameter values obtained from our fits to the data. Solving the equations for a known set of Raman shifts yields x_{Si} , y_{Sn} , and ϵ . Table 4 shows composition and in-plane strain values of the samples as fabricated in this work computed from the results of our Raman analysis. The largest deviations can be seen for Sample C. Here, Raman spectroscopy overestimates x_{Si} and underestimates y_{Sn} . One possible explanation for this is that for Sample C, the deviation of the composition from the lattice-matching condition (Figure S1) is larger than for all other samples. As a result, this sample features the largest strain. Indeed, for all samples, agreement of the Raman strain values with XRD measurements is poor. The reason is that the in-plane strain shift coefficients are difficult to determine. There are several different results in literature,^[24–26,28] and as for our values, large relative errors are specified.

TABLE 4 Comparison of composition and in-plane strain as measured by RBS/XRD and computed from the Raman results using the models developed here

4 | CONCLUSION

$\text{Si}_x\text{Ge}_{1-x-y}\text{Sn}_y$ layers with high Si content (up to $x = 0.46$) were grown by MBE and subjected to a Raman analysis. We used information obtained from RBS, TEM, EDXS, and XRD in order to measure composition and strain of each sample as a basis for the Raman analysis. Raman measurements obtained with an excitation wavelength of 633 nm provided us with spectra from which peak positions corresponding to the vibrational Ge–Ge, Si–Ge, and Si–Si modes could be extracted for all sample compositions. Taking all available data into account, we determined the coefficients for a set of empirical relations that are consistent with all measurement results and constitute a basis for the determination of a wide range of $\text{Si}_x\text{Ge}_{1-x-y}\text{Sn}_y$ alloy composition and strain, based on a Raman analysis alone. Our results extend previous analyses to ternary alloys with high Si content. They do not hint at more complex dependencies between composition, structure, and Raman peaks than found previously but corroborate the validity of linear models for higher Si contents. Furthermore, we were able to determine in-plane strain coefficients directly from the experimental data on ternary alloys. Our analysis shows that Raman spectroscopy proves to be a valuable tool for rapid nondestructive characterization of $\text{Si}_x\text{Ge}_{1-x-y}\text{Sn}_y$ alloys.

ACKNOWLEDGEMENTS

The authors acknowledge the support from Deutsche Forschungsgemeinschaft under Grants FI 1511/4-1, CA 1474/3-1, and KO 2911/13-1. They would like to thank

N. von den Driesch and D. Buca at Forschungszentrum Jülich for very helpful discussions.

Open access funding enabled and organized by Projekt DEAL.


ORCID

Jon Schlipf  <https://orcid.org/0000-0001-7929-5750>

Henriette Tetzner  <https://orcid.org/0000-0001-8400-5519>

Davide Spirito  <https://orcid.org/0000-0002-6074-957X>

Costanza L. Manganelli  <https://orcid.org/0000-0002-4218-2872>

Giovanni Capellini  <https://orcid.org/0000-0002-5169-2823>

Christoph T. Koch  <https://orcid.org/0000-0002-3984-1523>

Caterina J. Clausen  <https://orcid.org/0000-0002-8950-5990>

Stefano Chiussi  <https://orcid.org/0000-0002-3933-8725>

Inga A. Fischer  <https://orcid.org/0000-0003-3527-0716>

REFERENCES

- [1] R. Xie, P. Montanini, K. Akarvardar, N. Tripathi, B. Haran, S. Johnson, T. Hook, B. Hamieh, D. Corliss, J. Wang, X. Miao, J. Sporre, J. Fronheiser, N. Loubet, M. Sung, S. Sieg, S. Mochizuki, C. Prindle, S. Seo, A. Greene, J. Shearer, A. Labonte, S. Fan, L. Liebmann, R. Chao, A. Arceo, K. Chung, K. Cheon, P. Adusumilli, H. P. Amanapu, Z. Bi, J. Cha, H. C. Chen, R. Conti, R. Galatage, O. Gluschenkov, V. Kamineni, K. Kim, C. Lee, F. Lie, Z. Liu, S. Mehta, E. Miller, H. Niimi, C. Niu, C. Park, D. Park, M. Raymond, B. Sahu, M. Sankarapandian, S. Siddiqui, R. Southwick, L. Sun, C. Surisetty, S. Tsai, S. Whang, P. Xu, Y. Xu, C. Yeh, P. Zeitzoff, J. Zhang, J. Li, J. Demarest, J. Arnold, D. Canaperi, D. Dunn, N. Felix, D. Gupta, H. Jagannathan, S. Kanakasabapathy, W. Kleemeier, C. Labelle, M. Mottura, P. Oldiges, S. Skordas, T. Standaert, T. Yamashita, M. Colburn, M. Na, V. Paruchuri, S. Lian, R. Divakaruni, T. Gow, S. Lee, A. Knorr, H. Bu, M. Khare, in 2016 IEEE International Electron Devices Meeting (IEDM), **2016**, 2.7.1.
- [2] D. Marris-Morini, V. Vakarin, J. M. Ramirez, Q. Liu, A. Ballabio, J. Frigerio, M. Montesinos, C. Alonso-Ramos, X. L. Roux, S. Serna, D. Benedikovic, D. Chrastina, L. Vivien, G. Isella, *Nano* **2018**, 7, 1781.
- [3] S. Wirths, R. Geiger, N. von den Driesch, G. Mussler, T. Stoica, S. Mantl, Z. Ikonik, M. Luysberg, S. Chiussi, J. M. Hartmann, H. Sigg, J. Faist, D. Buca, D. Grützmacher, *Nat. Photonics* **2015**, 9, 88.
- [4] P. Moontragoon, Z. Ikonić, P. Harrison, *Semicond. Sci. Technol.* **2007**, 22, 742.
- [5] G. Han, S. Su, C. Zhan, Q. Zhou, Y. Yang, L. Wang, P. Guo, W. Wei, C. P. Wong, Z. X. Shen, B. Cheng, Y. C. Yeo, in 2011 IEEE International Electron Devices Meeting, **2011**, 16.7.1.
- [6] R. T. Beeler, D. J. Smith, J. Kouvetakis, J. Menéndez, *IEEE J. Photovolt.* **2012**, 2, 434.
- [7] I. A. Fischer, T. Wendav, L. Augel, S. Jitpakdeebodin, F. Oliveira, A. Benedetti, S. Stefanov, S. Chiussi, G. Capellini, K. Busch, J. Schulze, *Opt. Express* **2015**, 23, 25048.
- [8] V. R. D'Costa, Y.-Y. Fang, J. Tolle, J. Kouvetakis, J. Menéndez, *Phys. Rev. Lett.* **2009**, 102, 107403.
- [9] T. Wendav, I. A. Fischer, M. Montanari, M. H. Zoellner, W. Klesse, G. Capellini, N. von den Driesch, M. Oehme, D. Buca, K. Busch, J. Schulze, *Appl. Phys. Lett.* **2016**, 108, 242104.
- [10] C. J. Clausen, I. A. Fischer, D. Weisshaupt, F. Baerwolf, B. Tillack, G. Colston, M. Myronov, M. Oehme, J. Schulze, *Semicond. Sci. Technol.* **2018**, 33, 124017.
- [11] S. Wirths, D. Buca, S. Mantl, *Prog. Cryst. Growth Charact. Mater.* **2016**, 62, 1.
- [12] T. Yamaha, O. Nakatsuka, S. Takeuchi, W. Takeuchi, N. Taoka, K. Araki, K. Izunome, S. Zaima, *ECS Trans.* **2013**, 50, 907.
- [13] I. A. Fischer, A. Berrier, F. Hornung, M. Oehme, P. Zaumseil, G. Capellini, N. von den Driesch, D. Buca, J. Schulze, *Semicond. Sci. Technol.* **2017**, 32, 124004.
- [14] V. R. D'Costa, J. Tolle, C. D. Poweleit, J. Kouvetakis, J. Menéndez, *Phys. Rev. B* **2007**, 76, 035211.
- [15] J.-H. Fournier-Lupien, S. Mukherjee, S. Wirths, E. Pippel, N. Hayazawa, G. Mussler, J. M. Hartmann, P. Desjardins, D. Buca, O. Moutanabbir, *Appl. Phys. Lett.* **2013**, 103, 263103.
- [16] C. Xu, C. L. Senaratne, R. J. Culbertson, J. Kouvetakis, J. Menéndez, *J. Appl. Phys.* **2017**, 122, 125702.
- [17] O. Madelung (Ed), *Semiconductors: Group IV Elements and III-V Compounds*, Springer-Verlag, Berlin Heidelberg **1991**.
- [18] D. E. Aspnes, A. A. Studna, *Phys. Rev. B* **1983**, 27, 985.
- [19] H. K. Shin, D. J. Lockwood, J.-M. Baribeau, *Solid State Commun.* **2000**, 114, 505.
- [20] V. I. Korepanov, D. M. Sedlovets, *Analyst* **2018**, 143, 2674.
- [21] P. H. C. Eilers, *Anal. Chem.* **2003**, 75, 3631.
- [22] P. H. C. Eilers, H. Boelens, Unpublished. **2005**.
- [23] D. W. Marquardt, *J. Soc. Ind. Appl. Math.* **1963**, 11, 431.
- [24] J. S. Reparaz, A. Bernardi, A. R. Goñi, M. I. Alonso, M. Garriga, *Appl. Phys. Lett.* **2008**, 92, 081909.
- [25] J. C. Tsang, P. M. Mooney, F. Dacol, J. O. Chu, *J. Appl. Phys.* **1994**, 75, 8098.
- [26] F. Cerdeira, C. J. Buchenauer, F. H. Pollak, M. Cardona, *Phys. Rev. B* **1972**, 5, 580.
- [27] A. Gassenq, L. Milord, J. Aubin, N. Pauc, K. Guillois, J. Rothman, D. Rouchon, A. Chelnokov, J. M. Hartmann, V. Reboud, V. Calvo, *Appl. Phys. Lett.* **2017**, 110, 112101.
- [28] D. J. Lockwood, J.-M. Baribeau, *Phys. Rev. B* **1992**, 45, 8565.

SUPPORTING INFORMATION

Additional supporting information may be found online in the Supporting Information section at the end of this article.

How to cite this article: Schlipf J, Tetzner H, Spirito D, et al. Raman shifts in MBE-grown $\text{Si}_x\text{Ge}_{1-x-y}\text{Sn}_y$ alloys with large Si content. *J Raman Spectrosc.* 2021;1–9. <https://doi.org/10.1002/jrs.6098>